Design of Effective Catalysts for Selective Alkyne Hydrogenation by Doping of Ceria with a Single-Atom Promotor

Christopher Riley,[†,⊥] Shulan Zhou,[‡,§,⊥] Deepak Kunwar,[†,⊥] Andrew De La Riva,[†] Eric Peterson,[†] Robin Payne,[†] Liye Gao,[∥] Sen Lin,*,[‡,∥] Hua Guo,*,[‡] and Abhaya Datye*,[†]

[†]Department of Chemical and Biological Engineering and Center for Microengineered Materials, University of New Mexico, Albuquerque, New Mexico 87131, United States
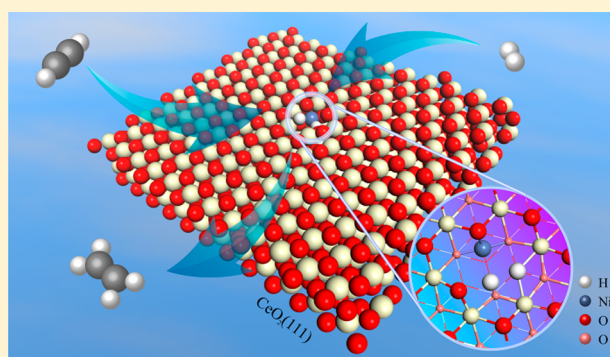
[‡]Department of Chemistry and Chemical Biology, University of New Mexico, Albuquerque, New Mexico 87131, United States

[§]Department of Material Science and Engineering, Jingdezhen Ceramic Institute, Jingdezhen 333403, China

[∥]State Key Laboratory of Photocatalysis on Energy and Environment, College of Chemistry, Fuzhou University, Fuzhou 350002, China

Ⓢ *Supporting Information*

ABSTRACT: Since the discovery that ceria is an active catalyst for selective hydrogenation of alkynes, there has been much debate on the catalytic mechanism. In this work, we propose, based on density functional theory (DFT) investigations, a mechanism that involves the heterolytic dissociation of H_2 at oxygen vacancies of $CeO_2(111)$, facilitated by frustrated Lewis pairs consisting of spatially separated O and Ce sites. The resulting O−H and Ce−H species effectively catalyze the hydrogenation of acetylene, avoiding the overstabilization of the C_2H_3* intermediate in a previously proposed mechanism. On the basis of our mechanism, we propose the doping of ceria by Ni as a means to create oxygen vacancies. Interestingly, the Ni dopant is not directly involved in the catalytic reaction, but

serves as a single-atom promoter. Experimental studies confirm the design principles and demonstrate much higher activity for Ni-doped ceria in selective hydrogenation of acetylene. The combined results from DFT calculations and experiment provide a basis to further develop selective hydrogenation catalysts based on earth-abundant materials.

1. INTRODUCTION

The partial hydrogenation of alkynes to olefin is widely used to purify olefin streams that usually contain acetylenic (e.g., acetylene) compounds as byproducts from steam cracking.[1] Traditionally, palladium catalysts are used to hydrogenate the acetylene to ethylene, but they overhydrogenate ethylene to ethane and oligomerize the corresponding hydrocarbons, thus creating undesired products.[1] Several factors have been identified to mitigate overhydrogenation. For example, Borodziński found that carbonaceous deposits on the palladium surface can sterically hinder ethylene from adsorbing and thus prevent ethylene hydrogenation.[2] Overhydrogenation may also be prevented by weakening ethylene adsorption because overhydrogenation typically occurs when desorption of ethylene from the catalyst surface is less energetically favorable than the hydrogenation ethylene to ethane. To this end, Studt et al. showed that these energies are comparable on a Pd(111) surface, leading to poor selectivity on palladium catalysts.[3] In addition, the formation of a Pd β-hydride phase via incorporation of subsurface hydrogen results in poor selectivity, likely due to an abundance of readily available hydrogen. Disruption of β-hydride phase formation, either

through use of small Pd particles or dopant atoms, can improve ethylene selectivity.[4,5]

A common approach, therefore, to improve ethylene selectivity is to alloy palladium with other metals. In doing so, active palladium atoms are dispersed over bimetallic nanoparticle surfaces, which can both disrupt formation of the β-hydride phase and weaken ethylene adsorption.[3,6] Alloying active metals often lowers overall activity, but does increase ethylene selectivity.[7] One disadvantage of this technique is that the metals incorporated into the catalyst, such as gold,[8,9] silver,[7] and gallium,[10] are expensive. Another issue is that bimetallic hydrogenation catalysts have been shown to phase separate under reaction conditions, or during regeneration under oxidizing conditions, which can negate the benefits of alloying.[9,11]

The present investigation explores the design of an inexpensive and selective alternative to conventional palladium catalysts. Our work is stimulated by the remarkable report that ceria (CeO_2) shows high activity and selectivity in catalyzing

the hydrogenation of alkyne to alkenes.[12−16] Ceria, which is relatively inexpensive, has attracted much recent attention due to its unique redox and acid−base properties associated with its high capacity to form oxygen vacancies.[17] The ceria-catalyzed hydrogenation requires relatively high temperatures (>500 K),[12] which signifies a substantial energy barrier. Doping of metal atoms in ceria is seen as a possible route to promote the catalytic activity.[18] However, our ability to design doped ceria as hydrogenation catalysts is hindered by the poor knowledge of catalytic mechanism.

To answer this challenge, several density functional theory (DFT) studies have been performed aimed at elucidation of the reaction mechanism. Carrasco et al., for example, proposed a mechanism that involved the initial H_2 dissociation on ceria surfaces followed by hydrogenation of the alkyne.[19] Although the former was proposed as the rate-limiting step, their mechanism involves a $C_2H_3^*$ intermediate that is about 4 eV below the reactant energy. The barrier for the final formation of ethylene ($C_2H_3^* + H^* \rightarrow C_2H_4$) is about 3 eV, which is kinetically infeasible. An alternative mechanism involves a concerted reaction between coadsorbed alkyne and H_2,[20] which also has a high barrier of ∼2 eV. In addition, it carries a heavy entropic penalty due to the weak adsorption energies of both species.

Although it is generally agreed that the dissociation of H_2 on oxide surfaces provides the hydrogen source for the hydrogenation reactions, the precise mechanism is still hotly debated. The heterolytic pathway generates both the surface O−H and Ce−H hydride species,[21,22] whereas the homolytic mechanism leads to the formation of two surface O−H species.[23−25] Both the O−H and Ce−H species can in principle be identified using IR spectroscopy, but so far only O−H species has been observed.[26] It is only very recently that the Ce−H hydride species was identified unambiguously via in situ neutron scattering spectroscopy.[27] Furthermore, the neutron scattering study revealed that the heterolytic dissociation only occured in the presence of oxygen vacancies in ceria. Another independent study also found evidence of the Ce−H hydride species upon H_2 dissociation on ceria in the presence of oxygen vacancies.[28] This can be readily understood as the Ce sites become exposed at oxygen vacancies, accompanied by the $Ce^{4+} \rightarrow Ce^{3+}$ reduction.[29] The resulting O and Ce sites on ceria surfaces can form the so-called frustrated Lewis pairs (FLPs),[30] because the acid and base sites are not adjunct to each other with a large separation in space.[31] The FLP differs from the more commonly seen classical Lewis pairs (CLPs), which are made up of adjunct acid−base sites. FLPs provide significant stabilization of the Ce−H hydride species, and facilitate the heterolytic H−H scission.

The mechanism proposed by Carrasco et al. involves homolytic dissociation of H_2, which forms two O−H species on the defect-free $CeO_2(111)$ surface.[19] Their DFT calculations indicated that this step has a significant (∼1 eV) barrier, but releases a large amount (2.35 eV) of energy, thanks to the stability of the O−H species. This sets the stage for the exceedingly high barrier in the formation of the ethylene product from the $C_2H_3^*$ intermediate, due apparently to the difficult transfer of the H atom from a surface OH group to the $C_2H_3^*$ species separated by more than 4 Å. As a result, it seems doubtful that the homolytic dissociation mechanism is viable.

Very recently, an alternative catalytic mechanism has been proposed by Huang et al.,[32] which involves an initial heterolytic dissociation of H_2 at oxygen vacancies on the $CeO_2(110)$ and $CeO_2(100)$ surfaces, leading to a surface O−H species and a ceria-bound Ce−H hydride. The surface vacancies form FLPs,[31] which enhance the heterolytic H−H bond scission. The subsequent hydrogenation of acetylene thus avoids the overstabilized $C_2H_3^*$ intermediate in the reaction pathway proposed by Carrasco et al.[19] As a result, this mechanism has a more reasonable reaction path and a much lower barrier for the formation of ethylene. As mentioned above, the existence of cerium hydride on ceria surfaces with O-vacancies has recently been verified experimentally,[27,28] thus providing key support for this mechanism.

Experimentally, it is established that the alkyne hydrogenation is catalyzed by the low-vacancy (111) face of ceria,[13] which is the most abundant facet due to its lowest surface energy.[33] Hence, the mechanism proposed by Huang et al.[32] for $CeO_2(100)$ and $CeO_2(110)$ may not apply. In this work, we propose a similar mechanism on the $CeO_2(111)$ surface, assuming the presence of some oxygen vacancies. The presence of such vacancies is well established even on "perfect" crystalline faces of CeO_2, particularly in the presence of H_2.[34,35] This mechanism calls for the initial heterolytic dissociation of H_2, forming O−H and Ce−H species at the oxygen vacancy (O_v), followed by sequential hydrogenation of acetylene.

Because the number of oxygen vacancies on $CeO_2(111)$ is typically very small, it is thus desirable to create such vacancies in order to increase the number of active sites and enhancing the reactivity. On the basis of the mechanism proposed here, we suggest the use of Ni doping of ceria as a way to help the semihydrogenation of acetylene. Like palladium, metallic nickel is an unselective acetylene hydrogenation catalyst, due in part to its high acetylene adsorption energy, which leads to oligomerization of acetylene.[36] However, the Ni dopant used here is in ionic form, largely designed to promote the formation of oxygen vacancies on ceria surfaces.[29,37] Multiple experimental studies have reported successful homogeneous incorporation of nickel into ceria,[38−43] but none has tested the catalytic activity in alkyne hydrogenation. Interestingly, the Ni-doped $CeO_2(111)$ (denoted as Ni@$CeO_2(111)$) is shown by our DFT calculations to lower the reaction barriers of hydrogenation steps. This prediction is borne out experimentally with a synthesized Ni-doped ceria catalyst, which catalyzes the hydrogenation of acetylene selectively to ethylene at a much lower light-off temperature than that on bare ceria surfaces. This synergistic study thus presents an exemplar for designing effective catalysts using both theoretical and experimental knowledge.

2. METHODS

2.1. Computational. All calculations were performed within spin-polarized DFT as implemented in the Vienna Ab initio Simulation Package (VASP).[44,45] The exchange-correlation potential was treated by the Perdew−Burke−Ernzerhof (PBE) gradient-corrected approximation.[46] van der Waals corrections were included using the DFT-D3 method of Grimme.[47] The core electrons were described by projector augmented-wave (PAW) method[48] and the valence electronic wave functions were expanded in plane waves up to a cutoff energy of 400 eV. In order to better describe the behavior of Ce f electrons, the DFT+U method with $U = 4.5$ eV[37,49,50] was employed. In this approach, a Hubbard U-like term describing the onsite Coulomb interactions was added to the generalized-gradient approximation (GGA) functional. This term is necessary in order to describe the f electron localization at oxygen vacancies on ceria
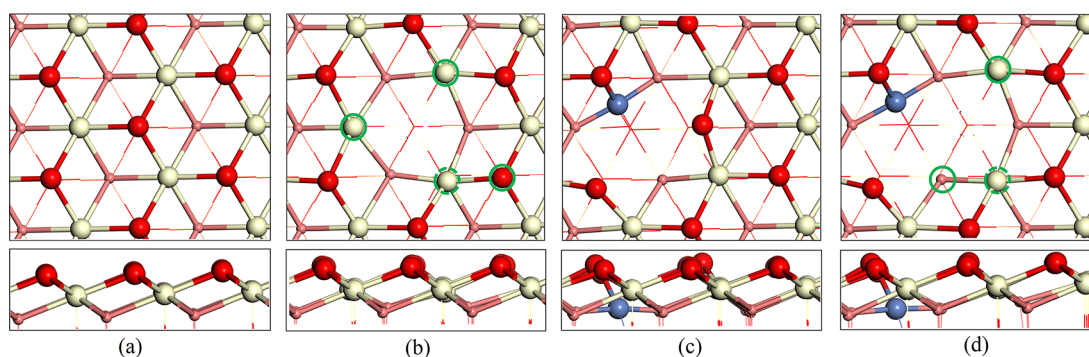
Figure 1. Top and side views of (a) $CeO_2(111)$, (b) $CeO_2(111)$-O_v, (c) Ni@$CeO_2(111)$, and (d) Ni@$CeO_2(111)$-O_v. Color scheme: Ni, blue; Ce, yellow; surface oxygen, red, second layer oxygen, light red. The FLPs are indicated in the figure by Ce and O sites in full green circles, whereas the CLP by the Ce site with a dashed green circle.

surfaces.[51,52] It should be noted that thermodynamics and kinetic parameters might require different U values.[53]

The O-terminated $CeO_2(111)$ surface was modeled by a 3×3 nine-atomic-layer supercell with the bottom three layers fixed. An O_v was created in the top layer of $CeO_2(111)$ by removing a lattice oxygen atom, corresponding to a concentration of O_v of about 1.85%. For the Ni-doped CeO_2 model, one surface Ce per unit cell was replaced by Ni. The substitution of Ce atom on the second atomic layer by Ni atom led to a large distortion of geometry. The formation of a square planar arrangement for Ni resulted in two 2-fold oxygen atoms which were unstable. The formation of the first O_v was spontaneous due to charge balance as a Ce^{4+}–O^{2-} pair on $CeO_2(111)$ was replaced by a Ni^{2+}–O_v pair.[29] This was confirmed by the exothermic formation energy of -0.42 eV, as opposed to the endothermic one (2.57 eV) on bare $CeO_2(111)$, in agreement with the previous theoretical results.[54] The formation of the second O_v required a larger formation energy of 1.49 eV.

A vacuum space of 14 Å in the z direction was used between the periodic images. The Brillouin zone was sampled at Γ-point, which is tested to converge.[55] The convergence of relaxation was checked with a 0.05 eV/Å criterion and the total energy difference was less than 10^{-4} eV. The adsorption energy of pertinent species was computed as follows: $E_{ads} = E_{(adsorbate+surface)} - E_{(free\ molecule)} - E_{(free\ surface)}$. The transition states (TSs) were determined using the climbing image nudged elastic band (CI-NEB) method,[56] and the reaction energy is defined as the energy difference between the initial state (IS) and final state (FS), and the activation energy as the energy difference between IS and TS. Vibrational analysis was further used to confirm the TS with only one imaginary frequency. The formation energy (E_f) of an O_v was calculated by the equation $E_f = E_{(defect)} - E_{(perfect)} - E_{(1/2O_2)}$. Here, $E_{(perfect)}$ was the energy of $CeO_2(111)$ or Ni@$CeO_2(111)$, whereas $E_{(defect)}$ was the energy of those with O_v. For the second O_v, the formation energy was relative to $CeO_2(111)$ and Ni@$CeO_2(111)$ with one oxygen already removed.

2.2. Experimental. Ceria and nickel-doped ceria samples were synthesized and tested for the acetylene hydrogenation reaction to examine the effects of nickel incorporation. In the nickel-doped ceria sample, care was taken to create isolated, homogeneously distributed nickel dopants. Such a structure is representative of our proposed mechanism, whereas nickel oxide and metallic nickel phases are not. Two synthesis techniques were utilized to prepare Ni-doped samples, coprecipitation and a mixed nitrate synthesis. Low nickel loadings were used (0.5, 1.0, and 1.5 wt % Ni) to ensure that all the Ni was doped into the lattice of ceria. To make the coprecipitated samples, appropriate amounts of cerium(III) nitrate hexahydrate (Aldrich, 99% trace metals basis) and nickel(II) nitrate hexahydrate (Alpha Aesar, 99.9985%) were dissolved into 100 mL of deionized (DI) water under vigorous stirring. A 1 M solution of potassium hydroxide (EDM Millipore) was added to the precursor solution to raise the pH to 10. Additional KOH was added to maintain pH > 9 for 1 h. The recovered precipitate was repeatedly rinsed with deionized water,

dried at 110 °C overnight, and calcined at 500 °C for 2 h. The mixed nitrate synthesis involved dissolution of appropriate amounts of cerium and nickel nitrates into DI water under vigorous stirring. The metal nitrate solutions were dried overnight at 110 °C to form a gel. The gel was then calcined at 500 °C for 2 h. The ceria sample (CeO_2) was prepared by calcining cerium nitrate at 500 °C for 2 h. Nickel oxide (NiO) and metallic nickel (Ni^0) were also synthesized as standards for XPS analysis. Nickel nitrate was calcined at 500 °C to form the NiO standard. Then, an aliquot of NiO was reduced in flowing H_2 at 500 °C for 1 h to form Ni^0. The sample was cooled to room temp in flowing H_2, purged with N_2, and then passivated upon air exposure. Surface oxide was removed through sputtering prior to analysis.

Catalyst samples were characterized via electron probe micro-analysis (EPMA), Brunauer–Emmett–Teller (BET) surface area determination, X-ray diffraction (XRD), transmission electron microscopy (TEM), and X-ray photoelectron spectroscopy (XPS). EPMA analysis measured nickel loading of the Ni@CeO_2 samples. A JEOL JXA-8200 Superprobe WD/ED combined microanalyzer was used to perform elemental analysis. Surface area measurements were obtained with a Micromeritics Gemini 2360 Surface Area Analyzer using liquid N_2 as coolant. A Rigaku SmartLab diffractometer with D/ TeX detector was used for XRD measurements. The CeO_2 and Ni@ CeO_2 samples were spiked with a corundum standard to obtain accurate lattice parameter values. TEM imaging was performed with a JEOL JEM 2010F field emission microscope. XPS analysis provided information on the oxidation states of nickel in the Ni@CeO_2 (as-prepared and after reaction), NiO, and Ni^0 samples. Cerium spectra were also gathered from several samples to determine relative proportion of reduced cerium (Ce^{3+}), which is an indication of nickel doping and oxygen vacancy formation. Measurements were taken using a Kratos AXIS DLD Ultra photoelectron spectrometer with monochromatic Al K_α source at 225 W. Spectra were charge referenced to aliphatic carbon at 285.0 eV. Quantitative analysis was conducted using CasaXPS.
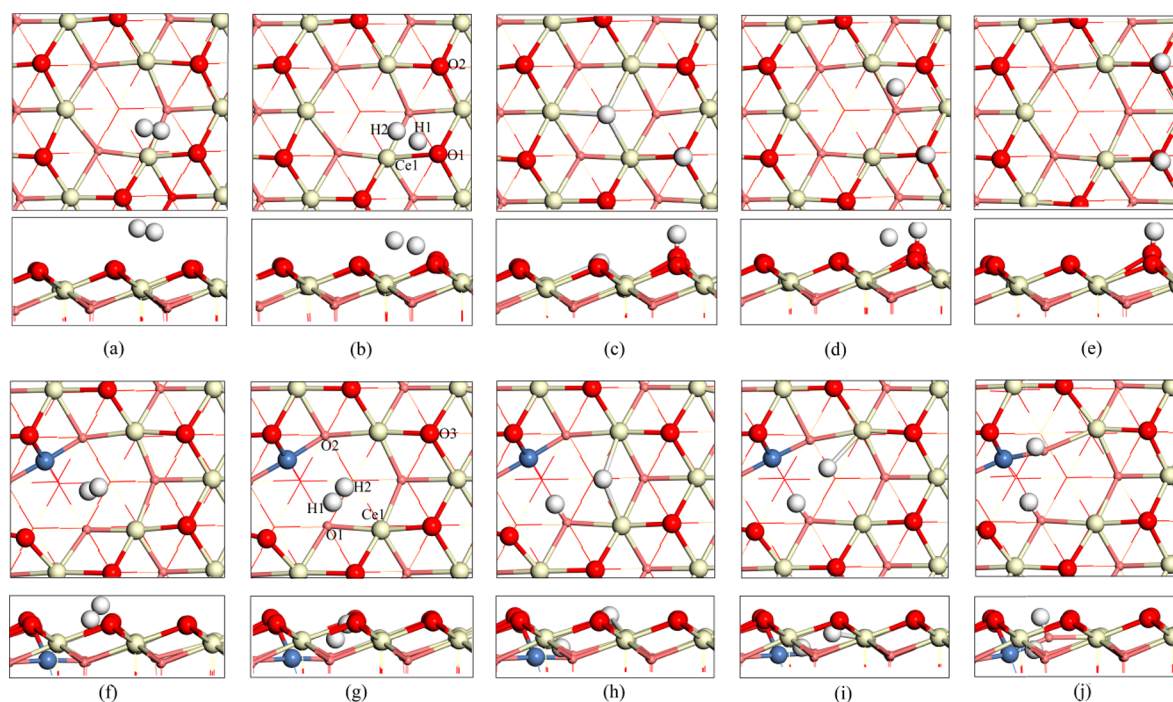
For reactivity measurements, the sieved catalyst was loaded into a glass reactor tube and held in place with glass wool plugs. Oxidation in flowing air and reduction in a flowing H_2/N_2 mixture were performed for 1 h each, both at 350 °C prior to testing for catalytic activity. A feed gas of 0.52% acetylene and 33.82% ethylene (balance N_2) at a flow rate of 70 mL/min and H_2 at a flow of 1.4 mL/min were used, giving an H_2 to C_2H_2 ratio of 3.85:1. Reaction data were also analyzed to determine activation energy and orders of reaction of acetylene and hydrogen.

3. RESULTS AND DISCUSSION

3.1. Mechanism of Hydrogenation of Acetylene on $CeO_2(111)$ with Oxygen Vacancies. The optimized geometries of $CeO_2(111)$ without and with the O_v, denoted respectively as $CeO_2(111)$ and $CeO_2(111)$-O_v, are shown in Figure 1a,b. As shown in Figure 1a, all Ce sites are connected

Table 1. Reaction Energies (ΔE in eV), Activation Energies (E_a in eV), and Imaginary Frequencies (cm^{-1}) of the Transition States for the Elementary Steps Involved in the H_2 Dissociation and C_2H_2 Hydrogenation

	$CeO_2(111)$-O_v			$Ni@CeO_2(111)$-O_v		
Reactions	ΔE	E_a	imaginary frequency	ΔE	E_a	imaginary frequency
$H_2 + * \rightarrow H_2*$	−0.19	−		−0.25	−	
$H_2* \rightarrow H*{-}O + H*{-}Ce$	−0.56	0.52	1098.2	−0.05	0.50	1021.3
$H*{-}O + H*{-}Ce \rightarrow 2H*{-}O$	−1.47	1.64	330.7	−1.47	0.87	845.3
$C_2H_2 + 2H* + * \rightarrow C_2H_2* + 2H*$	−0.30	−		−0.37	−	
$C_2H_2* + 2H* \rightarrow C_2H_3* + H*$	−1.62	0.37	188.2	−1.76	0.13	143.4
$C_2H_3* + H* \rightarrow C_2H_4*$	−0.29	0.70	1060.6	−0.56	0.62	1289.0

Figure 2. Top and side views of geometries of (a) H_2 adsorption (H_2*), (b) TS of the H_2 dissociation, (c) heterolytic products ($H*{-}Ce + H*{-}$O), (d) TS of $H*{-}Ce$ migration, (e) homolytic products ($H*{-}O + H*{-}O$) on $CeO_2(111)$-O_v, (f) H_2 adsorption (H_2*), (g) TS of H_2 dissociation, (h) heterolytic product ($H*{-}Ce + H*{-}O$), (i) TS for $H*$ migration from Ce to O, and (j) homolytic product ($H*{-}O + H*{-}O$) on $Ni@CeO_2(111)$-O_v.

to adjunct O sites, and as a result they form the so-called CLPs. From Figure 1b, it can be seen that the O_v formation on CeO_2 (111) leads to three six-coordinated Ce sites, which are more exposed than those in the absence of the O_v. Previous work has shown that the f electrons of the cerium atoms are localized in and near the O_v, thus changing their electronic characters.[51,52] As discussed extensively in the recent literature,[31] two exposed Ce sites and a nearby O, as indicated in the figure by full green circles, form two FLPs, while the Ce site labeled by a dashed green circle forms a CLP. These acid−base species in FLPs are not directly connected, and thus capable of catalyzing the heterolytic hydrogenation of H_2.

The dissociation of H_2 on defect-free $CeO_2(111)$ is known to proceed with a barrier of ~1 eV irrespective of the homolytic or heterolytic mechanisms.[21−25] In the presence of an O_v, the three exposed Ce sites are capable of binding hydrides. Therefore, it is possible for H_2 dissociation to proceed via the following heterolytic mechanism on $CeO_2(111)$-O_v with a significantly lowered barrier, thanks to the existence of FLPs. The reaction energy, activation energy, and imaginary frequencies at the TS are shown in Table 1. The corresponding IS, TS, and FS geometries are displayed in

Figure 2a−e, and their coordinates are given in Supporting Information (SI). The dissociation starts from a weakly adsorbed H_2 (E_{ads} = −0.19 eV) near a Ce (IS). In TS, the bond length of H−H bond is elongated from 0.74 Å in its isolated state to 1.06 Å whereas the distance of H−Ce and H−O is about 2.37 and 1.24 Å, respectively, Finally, H−H bond is completely broken, leading to the formation of the Ce−H and O−H species (FS) with an energy release of −0.56 eV. The two FLP Ce−O pairs help to stabilize the TS and thus lower the activation barrier from ~1 eV on the defect-free $CeO_2(111)$ to 0.52 eV. A similar TS was seen in the DFT work of Huang et al. for $CeO_2(110)$ and $CeO_2(100)$,[32] where the presence of oxygen vacancies (also interpreted as FLPs) were shown to lower the barrier of hydrogen dissociation.

It has been argued that the H in the Ce−H hydride from H_2 dissociation on the defect-free $CeO_2(111)$ can diffuse to an oxygen site, thus forming homolytic products,[21] We have examined whether the migration of H from the Ce site to an O site can take place on $CeO_2(111)$-O_v. The reaction and activation energies for these processes are also presented in Table 1. For $CeO_2(111)$-O_v, the diffusion of the H atom from the Ce site to the O2 site ($H*{-}O + H*{-}Ce \rightarrow 2H*{-}O$) in

the first layer (see Figure 2c−e) has to overcome an energy barrier of 1.65 eV, indicating high stability of H adsorption on Ce site. Hence, the exposed Ce sites on $CeO_2(111)$-O_v play an important role in stabilizing the hydride species. The existence of Ce−H species in the presence of hydrogen gas is supported by recent experimental work.[27,28]

The subsequent hydrogenation of acetylene is investigated using the hydrogenated $CeO_2(111)$-O_v model discussed above. The calculated reaction path of C_2H_2 hydrogenation on $CeO_2(111)$-O_v is compared with that of Carrasco et al. on $CeO_2(111)$[19] in Figure 3 and the corresponding energies as
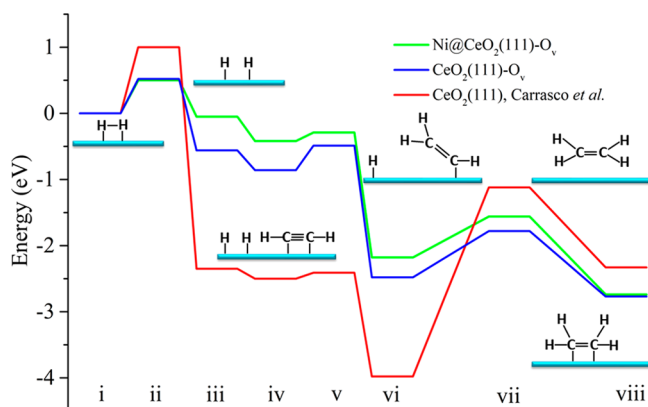

Figure 3. Calculated energy profiles of C_2H_2 hydrogenation on $CeO_2(111)$-O_v and Ni@$CeO_2(111)$-O_v with key species illustrated. The results on $CeO_2(111)$ calculated by Carrasco et al.[19] are also included for comparison. i, H_2*; ii, TS1; iii, 2H*; iv, C_2H_2* + 2H*; v, TS2; vi, C_2H_3* + H*; vii, TS3; viii, C_2H_4* (energy in the work of Carrasco et al. is for desorbed C_2H_2). Here * denotes the adsorption state.

well as the geometries are displayed in Table 1 and Figure 4, respectively. In the IS, C_2H_2 is initially adsorbed weakly at the O_v with a binding energy of about −0.30 eV. The first hydrogenation by the hydrogen bound at the Ce sites leads to a C_2H_3* intermediate with an energy barrier of 0.37 eV and an exothermicity of −1.62 eV. In the FS of this step, C_2H_3* is found to form mono-σ bonds to the two Ce sites with an adsorption energy of −1.97 eV. This intermediate species has been identified in the recent in situ DRIFTS study.[57] In the second hydrogenation step, the adsorbed C_2H_3* reacts further with another H from the surface O−H species to form C_2H_4*. The step requires a higher barrier of 0.70 eV, but it is significantly lower than that (2.86 eV) predicted by Carrasco et al.[19]

Obviously from Figure 3, the reaction barrier for the hydrogenation of the C_2H_3* intermediate on $CeO_2(111)$-O_v is significantly lower than that (2.86 eV) on the O sites in the model of Carrasco et al.,[19] showing that the exposed Ce sites on $CeO_2(111)$-O_v are more active. The decrease of the barrier can be explained by two factors. First, the C_2H_3* intermediate adsorbed on a Ce site instead of an O site avoids the cleavage of a strong C−O bond, which is highly endothermic. Second, during the reaction of C_2H_3* with H* adsorbed on an O site, the C atom and the H* species are very close to each other. As shown in Figure 4(d), in TS3, the H2−C2 distance is 1.50 Å. At the same time, C2 is still bound to Ce1 with a C2−Ce1 distance of 2.75 Å and the H2−O1 bond length is only elongated a little to 1.20 Å. This is completely different from situation in TS obtained by Carrasco et al.,[19] in which C and H have nearly no interaction with O ($d_{C−O}$ = 2.51 Å and $d_{H−O}$ = 2.24 Å) and the formation of C−H bond leads to a high barrier. This is also confirmed by their calculated large endothermicity (1.65 eV) of this step. The interaction between
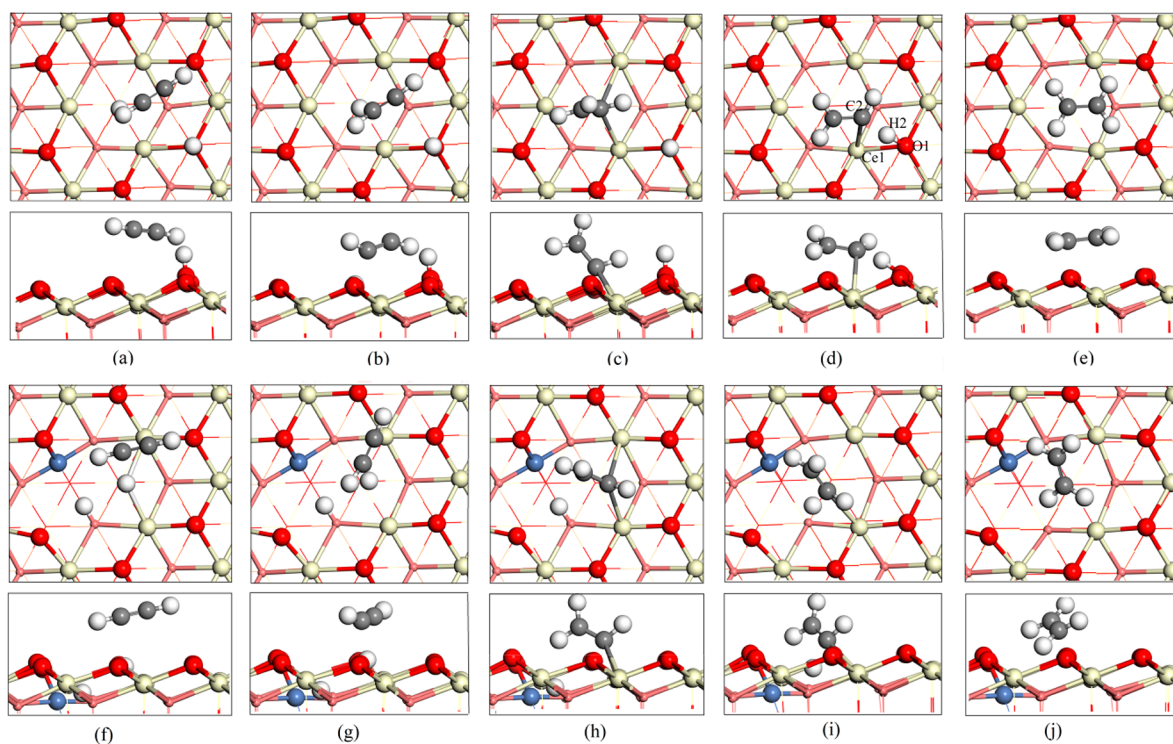

Figure 4. Top and side views of (a) 2H* + C_2H_2*, (b) TS2, (c) H* + C_2H_3*, (d) TS3, and (e) C_2H_4* on $CeO_2(111)$-O_v; (f) 2H* + C_2H_2*, (g) TS2, (h) H* + C_2H_3*, (i) TS3 and (j) C_2H_4* on Ni@$CeO_2(111)$-O_v.

H, C, O, and Ce no doubt helps stabilize the transition state, thus reducing the energy barrier.

On the other hand, our mechanism is quite similar to that found for the $CeO_2(110)$ and $CeO_2(100)$ by Huang et al.,[32] who also argued for the role of oxygen vacancies in catalyzing the hydrogenation of acetylene. Similarly, the H_2 dissociation on FLPs on these ceria facets proceeds via a heterolytic mechanism with low barriers, leading to stable hydrides at Ce sites. Their proposed reaction pathway also indicates that C_2H_2 hydrogenation initiates from attacking the hydride locating at Ce sites, avoiding the formation of a C−O bond. Furthermore, the adsorption energy of the C_2H_3* intermediate is much lower than that in the mechanism of Carrasco et al.,[19] resulting in a more moderate barrier for its final hydrogenation.

It should be noted that although the experiments by Pérez-Ramírez and co-workers[12,13] indicated that the (111) face of CeO_2 is more active than the (110) and (100) faces for the selective hydrogenation of acetylene, very little evidence was presented to support the notion that the number of oxygen vacancies on these CeO_2 surfaces is responsible for the differences in activity. Given the large calculated barrier for defect-free $CeO_2(111)$[19] and the latest in situ neutral scattering experiment,[27] oxygen vacancies are almost certainly involved in the catalysis.

To understand the impact of high coverage H adsorption, the adsorption of pertinent species is also explored. Under high coverage of H species, the adsorption energies of relevant species such as C_2H_2*, C_2H_3* and $H*$ on the Ce site of $CeO_2(111)−O_v$ are not significantly changed (from −0.30, −1.97, and −1.93 eV to −0.35, −2.29, and −2.28 eV, respectively). Therefore, the coverage effect is likely minor and is not further taken account in the study of the catalysis.

3.2. Mechanism of Hydrogenation of Acetylene on Ni@CeO$_2$(111) with Oxygen Vacancies. The aforementioned mechanism for acetylene hydrogenation on $CeO_2(111)$-O_v underscores the importance of the oxygen vacancies on $CeO_2(111)$, which exposes the Ce sites. Yet, the formation of oxygen vacancies on CeO_2 is not a spontaneous process. Indeed, the formation energy for an O_v on $CeO_2(111)$ is 2.57 eV, which is consistent with the previously reported values (2.60 eV).[49,58] The DFT value with the HSE06 (Heyd−Scuseria−Ernzerhof) hybrid functional is even larger (>3 eV),[51] indicating that the formation of an O_v is very difficult on the defect-free ceria surface. As a result, it is conceivable that an increase in oxygen vacancies on $CeO_2(111)$ could enhance the catalytic activity for semihydrogenation of alkynes.

Here, we propose a new catalyst for acetylene hydrogenation through doping ceria by an inexpensive transition metal, Ni. Ni doping of ceria has been reported before,[39−41] but mostly for hydrogen storage[38,59] and oxygenation.[42,43,60] To the best of our knowledge, however, no studies have focused on the catalytic properties of nickel ions incorporated into the ceria crystal lattice for use in selective alkyne hydrogenation, although selective alkyne hydrogenation catalyzed by Ga promoted CeO_2 has been recently reported.[18] Earlier theoretical work[54,61] has suggested the doping of divalent ions, such as Ni, in ceria helps to generate oxygen vacancies.

Our model for the Ni-doped $CeO_2(111)$ is shown in Figure 1c, in which one surface Ce is replaced by a Ni. The substitution leads to charge imbalance, and helps to form an O_v, which is denoted as Ni@CeO$_2$(111)-O_v and shown in Figure 1d. The formation of the O_v is spontaneous with a formation energy of −0.42 eV, which is in contrast to the

endothermicity (2.57 eV) of O_v formation on pure $CeO_2(111)$. In Figure 1d, Ni coordinates with four neighboring O, forming a stable square planar geometry. Like on $CeO_2(111)$-O_v, there exist both a FLP and a CLP, depending on whether the Ce site is adjunct to the O site. The Ce in the former is labeled by a full green circle and the latter by a dashed green circle.

On Ni@CeO$_2$(111)-O_v, H_2 dissociation can in principle take place through the homolytic path (Figure S6 in SI). This dissociation is highly exothermic (−2.20 eV) and the energy barrier is only 0.22 eV lower than that (∼1 eV) on $CeO_2(111)$ without O_v,[21,25] which can be explained by the fact that the interaction between H and Ni makes the geometry of TS more stable. These results are not significantly different from those on $CeO_2(111)$, but as discussed above, homolytic H−H scission leads to an overstabilized C_2H_3* intermediate,[19] which becomes kinetically infeasible. Thus, the subsequent reaction steps are not explored further.

We then explore the heterolytic pathway by first assuming one hydrogen is adsorbed on Ni. However, this configuration is unstable because Ni is saturated in the square planar geometry. This observation is quite interesting as it suggests that the Ni dopant is not directly involved in the catalysis. Rather, it promotes the formation of oxygen vacancies on ceria, which forms the active sites of the catalyst. As a result, it can be considered as a single-atom promotor. More importantly, the avoidance of H adsorption further shields the Ni^{2+} dopant from reduction to Ni^0, which may agglomerate to form metallic Ni clusters on the CeO_2 surface. When H_2 dissociates over the Ce/O pairs (consisting of one FLP and one CLP) following heterolytic mechanism, the process is quite similar to that on $CeO_2(111)$-O_v. The relevant energies and geometries are shown in Table 1 and Figure 2f−j, respectively. In the IS, H_2 weakly adsorbs near the O_v with the adsorption energy of −0.25 eV. The TS displays an increased H−H bond length of 1.02 Å and a shorten H−O distance of 1.27 Å. As shown in Figure 2g, both H1 and H2 atoms interact with the Ce1 atom with the H1−Ce1 and H2−Ce1 bond lengths of 2.33 and 2.45 Å, respectively. At the end, the cleavage of H−H bond results in the heterolytic products of Ce−H and O−H species on adjacent Ce and O sites, respectively. The calculated energy barrier is about 0.50 eV, much lower than that (0.78 eV) through the homolytic mechanism. This can be ascribed to the polarization caused by the exposed Ce and O atoms which helps the scission of H−H bond. The reduced barrier indicates that the exposed single Ce atom sites in the presence of O_v are more active than single Ni atom sites toward the dissociation of H_2. It should be noted the barrier is almost equal to that (0.52 eV) on $CeO_2(111)$-O_v without doping, suggesting a minor influence of Ni doping on the hydrogen bond scission.

To examine the possibility of H migration from the Ce site to an O site, two possible oxygen sites (O2 (surface oxygen) and O3 (subsurface oxygen) in Figure 2g) are considered. From the calculated results, the migration processes are exothermic, but the energy barriers of H transferring from Ce site to O2 and O3 sites (geometries of TSs are shown in Figure 2i and Figure S3a, respectively) are as high as 0.87 and 1.06 eV, respectively, implying that H is transiently stable at the exposed Ce sites. These results are consistent with the in situ neutron scattering experiment.[27]

For the hydrogenation reaction, C_2H_2 is found to weakly adsorb near the O_v with an adsorption energy of −0.37 eV (Figure 4). The first hydrogenation step (C_2H_2* + $H*$ →
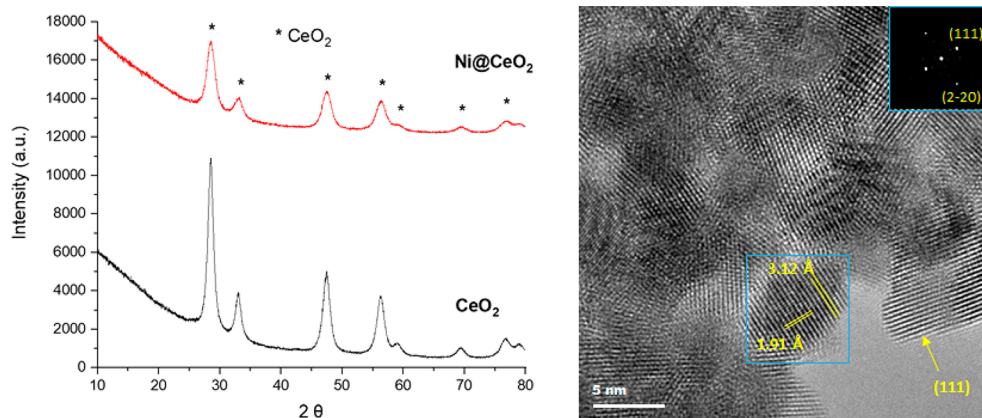
Figure 5. XRD patterns of CeO_2 and coprecipitated 1.5 wt % $Ni@CeO_2$ samples (left) and HRTEM image of the nickel-doped ceria sample (right). The inset shows a Fourier transform of the boxed region, showing the prominent (111) lattice planes and the faint (220) planes seen in the image. These particles expose well-defined (111) surfaces as indicated in the figure.
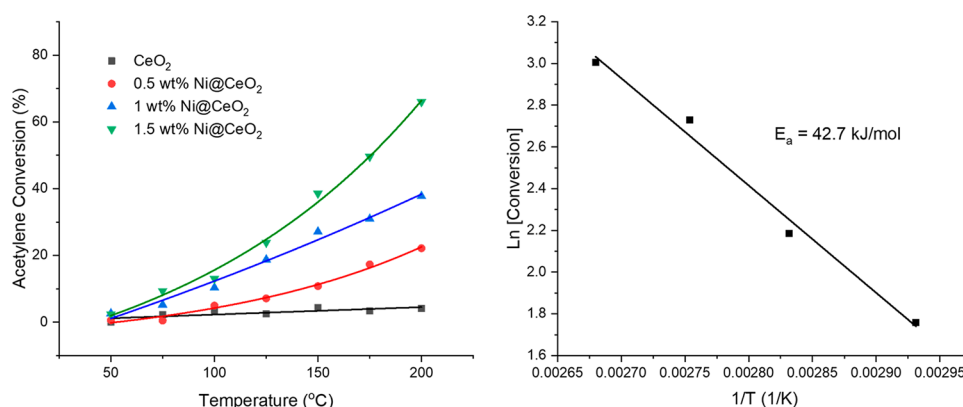

Figure 6. Acetylene hydrogenation reactivity for 0.5, 1.0, and 1.5 wt % $Ni@CeO_2$ mixed nitrate samples and CeO_2 shown as % conversion as a function of temperature (left panel) and Ln(conversion) as a function of 1/T of the 1.5 wt % $Ni@CeO_2$ mixed nitrate sample (right panel). The low reactivity of ceria is evident. No ethane was detected and ethylene was the only product in all of these measurements.

C_2H_3*) has a very small energy barrier of 0.13 eV, releasing −1.76 eV of energy. The resulting C_2H_3* species is adsorbed at the bridge sites of two exposed Ce atoms, very similar to the case of $CeO_2(111)$-O_v. The adsorption energy for C_2H_3* is only −1.43 eV. The second hydrogenation step from C_2H_3* to C_2H_4* needs to overcome a barrier of 0.62 eV, which is the rate-determining step of the hydrogenation reaction. When zero-point energies are included, the barrier becomes 0.53 eV. This barrier is lower than that (0.70 eV) on $CeO_2(111)$-O_v, indicating that Ni doping helps the catalysis.

It is also interesting to ask whether the oligomerization process can take place on $Ni@CeO_2(111)$-O_v. On one hand, it should be noted that the catalyst surface is covered by H species, which might hinder the adsorption of the intermediates of oligomerization. On the other hand, the Ni coordination is saturated as we discussed earlier, also preventing the intermediates of oligomerization from binding at the Ni sites. Thus, it is reasonable to assume that the oligomerization is a minor reaction on the H precovered $Ni@CeO_2(111)$-O_v. Further calculations will be carried out in the future to explore this issue.

3.3. Experimental Evidence. The $Ni@CeO_2$ samples showed that the nickel dopant was incorporated uniformly into the ceria structure. As shown in Figure 5, no nickel oxide or metallic nickel peaks were seen in the XRD pattern of 1.5 wt % $Ni@CeO_2$, the most intense of which would appear at 43.4°

and 44.5°, respectively. This demonstrates that no crystalline nickel phases exist in the sample. This is consistent with the theoretical model of Ni doping at the Ce sites. Lattice constants for ceria crystallites in the CeO_2 and $Ni@CeO_2$ samples were determined by adding a corundum standard as an internal reference. The constants for CeO_2 and 1.5 wt % $Ni@CeO_2$ samples are 5.4127(±0.0001) and 5.4096(±0.0002) Å, respectively (Figure S1 in SI). A contraction of the ceria lattice constant upon nickel incorporation is well documented as evidence of smaller nickel ions replacing cerium ions in the ceria crystal lattice.[38−40] Further, TEM imaging (Figure 5) shows only ceria lattice fringes; no separate nickel containing particles were detected. The prominent facet is $CeO_2(111)$, as expected. EPMA measured nickel composition to be 1.54 wt % in this $Ni@CeO_2$ sample, which is close to the nominal value. BET analysis shows the specific surface areas of CeO_2 and $Ni@CeO_2$ to be similar at 87.7 and 81.4 m^2/g, respectively.

The activity for acetylene hydrogenation on 0.5, 1.0, and 1.5 wt % $Ni@CeO_2$ mixed nitrate and CeO_2 samples is shown in Figure 6. Activity for coprecipitated 1.5 wt % $Ni@CeO_2$ is similar and shown in Figure S2 of SI. The $Ni@CeO_2$ sample is active for hydrogenation while CeO_2 achieves only minor acetylene conversions up to 200 °C. The Arrhenius plot in the same figure shows an apparent activation energy of 42.7 kJ/mol, which is very close to our calculated ZPE-corrected value
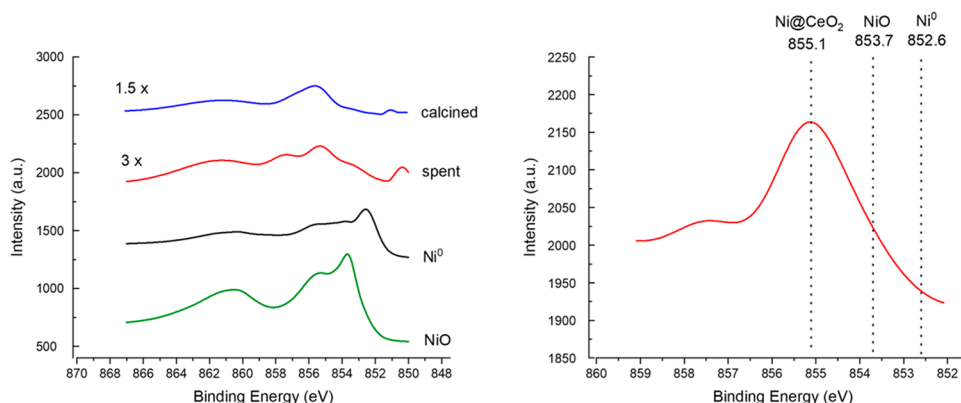
Figure 7. XPS spectra of nickel oxide, metallic nickel, and coprecipitated 1.5 wt % Ni@CeO$_2$ before reaction (calcined) and after reaction spent (left). An inset of spent Ni@CeO$_2$ with peak locations marked for NiO, Ni^0, and Ni as ceria dopant (right).

of 0.53 eV for C$_2$H$_3$* + H* → C$_2$H$_4$*. The lower reactivity for CeO$_2$ and the improved reactivity for Ni@CeO$_2$ corroborates our proposed mechanism, in which the energy barrier of hydrogenation on Ni@CeO$_2$ is found to be lower than that on CeO$_2$ (see Table 1 and Figure 3). The reason for the lower reactivity on CeO$_2$ might be that CeO$_2$ contains fewer active sites, due to limited number of oxygen vacancies. This is in agreement with our DFT results that on bare CeO$_2$(111), the formation energy of O$_v$ is as high as 2.57 eV. For Ni@CeO$_2$, nickel dopants incorporated into the ceria lattice encourage O$_v$ formation, which is confirmed by our calculated O$_v$ formation energy of −0.42 eV. Kinetic experiments show acetylene hydrogenation to be first order with respect to both hydrogen and acetylene on the Ni@CeO$_2$ samples (Figure S3 in SI).

The coprecipitated 1.5 wt % Ni@CeO$_2$ sample was analyzed via XPS before and after acetylene hydrogenation reaction to ensure that nickel dopants remained dispersed and did not form other nickel phases upon reduction and reaction. Figure 7 shows XPS spectra of these samples, as well as of NiO and Ni^0 for reference (left). The figure on the right shows an inset of the spent Ni@CeO$_2$ sample spectra with labeled peak positions corresponding to metallic nickel (852.6 eV), nickel oxide (853.7 eV), and the prominent peak (855.1 eV) which we have assigned to Ni@CeO$_2$. Davidson et al. attributed this peak to nickel doped into the ceria structure, with the peak position between 855.0 and 855.5 eV, depending on calcination temperature.[62] Even after reduction and hydrogenation reactions, Ni continues to exist as a dopant in the ceria lattice, consistent with an earlier report that Ni is not reduced below 400 °C.[63] This is also consistent with our DFT calculation results that the structure of Ni@CeO$_2$(111) stays intact during both H$_2$ dissociation and acetylene hydrogenation processes (see Figure 2 and Figure 4). In other words, the Ni dopant in ceria resists reduction by hydrogen. XPS analysis also confirmed that the percentage of reduced cerium ions increased when ceria was doped with nickel (see Figure S4 in SI). This is expected as nickel dopants create charge-compensating oxygen vacancies and reduce neighboring cerium ions from 4+ to 3+ oxidation state (see SI). Further, XAS analysis of an even more highly loaded 3.65 wt % Ni@CeO$_2$ sample does not show the presence of metallic nickel or nickel oxide phases (see Figure S5 in SI).

4. CONCLUSIONS

In this work, H$_2$ dissociation and C$_2$H$_2$ hydrogenation on CeO$_2$(111)-O$_v$ and Ni@CeO$_2$(111)-O$_v$ were systematically investigated by DFT calculations. The calculation results strongly suggest the prominent role of oxygen vacancies in the catalysis. It is shown that the removal of a surface oxygen creates exposed Ce sites, which can form frustrated Lewis pairs (FLPs)[31] with surface oxygens. The existence of FLPs at the O$_v$ stabilizes the transition state for heterolytic H$_2$ dissociation,[32] and the resulting C−H hydride species has recently been experimentally identified using in situ inelastic neutron scattering spectroscopy.[27] Indeed, the formation of hydride species on oxide surfaces might be more prevalent than realized before, as recent studies of several oxides revealed.[27,28,64,65] The involvement of hydride in the mechanism is the key to avoid the formation of the overstabilized C$_2$H$_3$* intermediate and the large kinetic barrier associated with its hydrogenation seen in a previously proposed mechanism.[19] This mechanism is similar to those recently proposed for hydrogenation of acetylene on CeO$_2$(100) and CeO$_2$(110).[32]

However, the formation of oxygen vacancies on CeO$_2$(111) is difficult, which is the likely reason for the high operating temperatures required for hydrogenation. To improve the catalytic activity, we proposed the doping of ceria with nickel, which leads to the ready formation of oxygen vacancies on CeO$_2$(111) and the exposure of single Ce atom sites. First-principles results suggest that the Ni doping lowers the barrier for the rate-limiting step for this reaction, but Ni does not participate in the catalysis directly. Its role is thus an indirect one, serving as a single-atom promotor to create and modify the active site. Furthermore, the avoidance of interacting with hydrogen is also responsible for the stability of the Ni^{2+} dopant in ceria and its resistance to reduction. To verify the theoretical results, uniform Ni-doped ceria samples are made and tested for selective hydrogenation of acetylene. It is shown that the new catalyst is active at much lower temperature, thus validating the theoretical prediction.

The combined theoretical−experimental results reported here have important implications in oxide catalyzed hydrogenation reactions. In particular, the importance of oxygen vacancies as the active sites for hydrogenation is consistent with the experimental and theoretical evidence for both ceria and other oxides.[12,13,66−71] Doping of divalent metals such as Ni is known to enhance the formation of oxygen vacancies on

ceria surfaces and thus the catalytic activity, as demonstrated here. This design principle could lead to more effective catalysts in the future.

■ ASSOCIATED CONTENT

Ⓢ Supporting Information

The Supporting Information is available free of charge on the ACS Publications website at DOI: 10.1021/jacs.8b07789.

Additional experimental and theoretical results (PDF)

■ AUTHOR INFORMATION

Corresponding Authors

*slin@fzu.edu.cn
*hguo@unm.edu
*datye@unm.edu

ORCID Ⓞ

Sen Lin: 0000-0002-2288-5415
Hua Guo: 0000-0001-9901-053X

Author Contributions

[⊥]These authors contributed equally.

Notes

The authors declare no competing financial interest.

■ ACKNOWLEDGMENTS

■ REFERENCES

(1) Bond, G. C. *Metal-Catalysed Reactions of Hydrocarbons*; Springer: New York, 2005.

(2) Borodziński, A. *Catal. Lett.* **1999**, *63*, 35.

(3) Studt, F.; Abild-Pedersen, F.; Bligaard, T.; Sørensen, R. Z.; Christensen, C. H.; Nørskov, J. K. *Science* **2008**, *320*, 1320.

(4) Teschner, D.; Borsodi, J.; Wootsch, A.; Révay, Z.; Hävecker, M.; Knop-Gericke, A.; Jackson, S. D.; Schlögl, R. *Science* **2008**, *320*, 86.

(5) Benavidez, A. D.; Burton, P. D.; Nogales, J. L.; Jenkins, A. R.; Ivanov, S. A.; Miller, J. T.; Karim, A. M.; Datye, A. K. *Appl. Catal., A* **2014**, *482*, 108.

(6) Khan, N. A.; Shaikhutdinov, S.; Freund, H. J. *Catal. Lett.* **2006**, *108*, 159.

(7) Pei, G. X.; Liu, X. Y.; Wang, A.; Lee, A. F.; Isaacs, M. A.; Li, L.; Pan, X.; Yang, X.; Wang, X.; Tai, Z.; Wilson, K.; Zhang, T. *ACS Catal.* **2015**, *5*, 3717.

(8) Choudhary, T. V.; Sivadinarayana, C.; Datye, A. K.; Kumar, D.; Goodman, D. W. *Catal. Lett.* **2003**, *86*, 1.

(9) Di Vece, M.; Bals, S.; Verbeeck, J.; Lievens, P.; Van Tendeloo, G. *Phys. Rev. B: Condens. Matter Mater. Phys.* **2009**, *80*, 125420.

(10) Osswald, J.; Giedigkeit, R.; Jentoft, R. E.; Armbrüster, M.; Girgsdies, F.; Kovnir, K.; Ressler, T.; Grin, Y.; Schlögl, R. *J. Catal.* **2008**, *258*, 210.

(11) Liu, H. B.; Pal, U.; Medina, A.; Maldonado, C.; Ascencio, J. A. *Phys. Rev. B: Condens. Matter Mater. Phys.* **2005**, *71*, 075403.

(12) Vilé, G.; Bridier, B.; Wichert, J.; Pérez-Ramírez, J. *Angew. Chem., Int. Ed.* **2012**, *51*, 8620.

(13) Vilé, G.; Colussi, S.; Krumeich, F.; Trovarelli, A.; Pérez-Ramírez, J. *Angew. Chem. Int. Ed.* **2014**, *53*, 12069.

(14) Vilé, G.; Wrabetz, S.; Floryan, L.; Schuster, M. E.; Girgsdies, F.; Teschner, D.; Pérez-Ramírez, J. *ChemCatChem* **2014**, *6*, 1928.

(15) Vilé, G.; Albani, D.; Almora-Barrios, N.; López, N.; Pérez-Ramírez, J. *ChemCatChem* **2016**, *8*, 21.

(16) Albani, D.; Shahrokhi, M.; Chen, Z.; Mitchell, S.; Hauert, R.; López, N.; Pérez-Ramírez, J. *Nat. Commun.* **2018**, *9*, 2634.

(17) Trovarelli, A. *Catalysis by Ceria and Related Materials*; Imperial College Press: London, 2002.

(18) Vilé, G.; Dähler, P.; Vecchietti, J.; Baltanás, M.; Collins, S.; Calatayud, M.; Bonivardi, A.; Pérez-Ramírez, J. *J. Catal.* **2015**, *324*, 69.

(19) Carrasco, J.; Vilé, G.; Fernández-Torre, D.; Pérez, R.; Pérez-Ramírez, J.; Ganduglia-Pirovano, M. V. *J. Phys. Chem. C* **2014**, *118*, 5352.

(20) García-Melchor, M.; Bellarosa, L.; López, N. *ACS Catal.* **2014**, *4*, 4015.

(21) García-Melchor, M.; López, N. *J. Phys. Chem. C* **2014**, *118*, 10921.

(22) Fernández-Torre, D.; Carrasco, J.; Ganduglia-Pirovano, M. V.; Pérez, R. *J. Chem. Phys.* **2014**, *141*, 014703.

(23) Sohlberg, K.; Pantelides, S. T.; Pennycook, S. J. *J. Am. Chem. Soc.* **2001**, *123*, 6609.

(24) Vicario, G.; Balducci, G.; Fabris, S.; de Gironcoli, S.; Baroni, S. *J. Phys. Chem. B* **2006**, *110*, 19380.

(25) Chen, H.-T.; Choi, Y. M.; Liu, M.; Lin, M. C. *ChemPhysChem* **2007**, *8*, 849.

(26) Binet, C.; Daturi, M.; Lavalley, J.-C. *Catal. Today* **1999**, *50*, 207.

(27) Wu, Z.; Cheng, Y.; Tao, F.; Daemen, L.; Foo, G. S.; Nguyen, L.; Zhang, X.; Beste, A.; Ramirez-Cuesta, A. J. *J. Am. Chem. Soc.* **2017**, *139*, 9721.

(28) Werner, K.; Weng, X.; Calaza, F.; Sterrer, M.; Kropp, T.; Paier, J.; Sauer, J.; Wilde, M.; Fukutani, K.; Shaikhutdinov, S.; Freund, H.-J. *J. Am. Chem. Soc.* **2017**, *139*, 17608.

(29) Paier, J.; Penschke, C.; Sauer, J. *Chem. Rev.* **2013**, *113*, 3949.

(30) Stephan, D. W.; Erker, G. *Angew. Chem. Int. Ed.* **2015**, *54*, 6400.

(31) Zhang, S.; Huang, Z.-Q.; Ma, Y.; Gao, W.; Li, J.; Cao, F.; Li, L.; Chang, C.-R.; Qu, Y. *Nat. Commun.* **2017**, *8*, 15266.

(32) Huang, Z.-Q.; Liu, L.-P.; Qi, S.; Zhang, S.; Qu, Y.; Chang, C.-R. *ACS Catal.* **2018**, *8*, 546.

(33) Trovarelli, A.; Llorca, J. *ACS Catal.* **2017**, *7*, 4716.

(34) Esch, F.; Fabris, S.; Zhou, L.; Montini, T.; Africh, C.; Fornasiero, P.; Comelli, G.; Rosei, R. *Science* **2005**, *309*, 752.

(35) Wu, Z.; Li, M.; Mullins, D. R.; Overbury, S. H. *ACS Catal.* **2012**, *2*, 2224.

(36) Trimm, D. L.; Liu, I. O. Y.; Cant, N. W. *J. Mol. Catal. A: Chem.* **2008**, *288*, 63.

(37) McFarland, E. W.; Metiu, H. *Chem. Rev.* **2013**, *113*, 4391.

(38) Wrobel, G.; Lamonier, C.; Bennani, A.; D'Huysser, A.; Aboukais, A. *J. Chem. Soc., Faraday Trans.* **1996**, *92*, 2001.

(39) Lamonier, C.; Ponchel, A.; D'Huysser, A.; Jalowiecki-Duhamel, L. *Catal. Today* **1999**, *50*, 247.

(40) Ponchel, A.; D'Huysser, A.; Lamonier, C.; Jalowiecki-Duhamel, L. *Phys. Chem. Chem. Phys.* **2000**, *2*, 303.

(41) Wang, L.; Zhang, S.; Liu, Y. *J. Rare Earths* **2008**, *26*, 66.

(42) Mahammadunnisa, S.; Manoj Kumar Reddy, P.; Lingaiah, N.; Subrahmanyam, C. *Catal. Sci. Technol.* **2013**, *3*, 730.

(43) Tang, K.; Liu, W.; Li, J.; Guo, J.; Zhang, J.; Wang, S.; Niu, S.; Yang, Y. *ACS Appl. Mater. Interfaces* **2015**, *7*, 26839.

(44) Kresse, G.; Furthmuller, J. *Phys. Rev. B: Condens. Matter Mater. Phys.* **1996**, *54*, 11169.

(45) Kresse, G.; Furthmuller, J. *Comput. Mater. Sci.* **1996**, *6*, 15.

(46) Perdew, J. P.; Burke, K.; Ernzerhof, M. *Phys. Rev. Lett.* **1996**, *77*, 3865.

(47) Grimme, S.; Antony, J.; Ehrlich, S.; Krieg, H. *J. Chem. Phys.* **2010**, *132*, 154104.

(48) Blöchl, P. E. *Phys. Rev. B: Condens. Matter Mater. Phys.* **1994**, *50*, 17953.

(49) Fabris, S.; Vicario, G.; Balducci, G.; de Gironcoli, S.; Baroni, S. *J. Phys. Chem. B* **2005**, *109*, 22860.

(50) Krcha, M. D.; Janik, M. J. *Int. J. Quantum Chem.* **2014**, *114*, 8.

(51) Ganduglia-Pirovano, M. V.; Da Silva, J. L. F.; Sauer, J. *Phys. Rev. Lett.* **2009**, *102*, 026101.

(52) Li, H.-Y.; Wang, H.-F.; Gong, X.-Q.; Guo, Y.-L.; Guo, Y.; Lu, G.; Hu, P. *Phys. Rev. B: Condens. Matter Mater. Phys.* **2009**, *79*, 193401.

(53) Capdevila-Cortada, M.; Łodziana, Z.; López, N. *ACS Catal.* **2016**, *6*, 8370.

(54) Nolan, M. *J. Mater. Chem.* **2011**, *21*, 9160.

(55) Monkhorst, H. J.; Pack, J. D. *Phys. Rev. B* **1976**, *13*, 5188.

(56) Henkelman, G.; Uberuaga, B. P.; Jónsson, H. *J. Chem. Phys.* **2000**, *113*, 9901.

(57) Cao, T.; You, R.; Zhang, X.; Chen, S.; Li, D.; Zhang, Z.; Huang, W. *Phys. Chem. Chem. Phys.* **2018**, *20*, 9659.

(58) Song, Y.-L.; Yin, L.-L.; Zhang, J.; Hu, P.; Gong, X.-Q.; Lu, G. *Surf. Sci.* **2013**, *618*, 140.

(59) Jalowiecki-Duhamel, L.; Debeusscher, S.; Zarrou, H.; D'Huysser, A.; Jobic, H.; Payen, E. *Catal. Today* **2008**, *138*, 266.

(60) Pino, L.; Vita, A.; Cipitì, F.; Laganà, M.; Recupero, V. *Catal. Lett.* **2008**, *122*, 121.

(61) Kehoe, A. B.; Scanlon, D. O.; Watson, G. W. *Chem. Mater.* **2011**, *23*, 4464.

(62) Davidson, A.; Tempere, J. F.; Che, M.; Roulet, H.; Dufour, G. *J. Phys. Chem.* **1996**, *100*, 4919.

(63) Barrio, L.; Kubacka, A.; Zhou, G.; Estrella, M.; Martínez-Arias, A.; Hanson, J. C.; Fernández-García, A.; Rodriguez, J. A. *J. Phys. Chem. C* **2010**, *114*, 12689.

(64) Chen, H.-Y. T.; Giordano, L.; Pacchioni, G. *J. Phys. Chem. C* **2013**, *117*, 10623.

(65) Vecchietti, J.; Baltanás, M. A.; Gervais, C.; Collins, S. E.; Blanco, G.; Matz, O.; Calatayud, M.; Bonivardi, A. *J. Catal.* **2017**, *345*, 258.

(66) Schimming, S. M.; Foo, G. S.; LaMont, O. D.; Rogers, A. K.; Yung, M. M.; D'Amico, A. D.; Sievers, C. *J. Catal.* **2015**, *329*, 335.

(67) Song, J.; Huang, Z.-F.; Pan, L.; Zou, J.-J.; Zhang, X.; Wang, L. *ACS Catal.* **2015**, *5*, 6594.

(68) Wu, X.-P.; Gong, X.-Q.; Lu, G. *Phys. Chem. Chem. Phys.* **2015**, *17*, 3544.

(69) Lu, J.; Song, J.; Niu, H.; Pan, L.; Zhang, X.; Wang, L.; Zou, J.-J. *Appl. Surf. Sci.* **2016**, *371*, 61.

(70) Albani, D.; Capdevila-Cortada, M.; Vilé, G.; Mitchell, S.; Martin, O.; López, N.; Pérez-Ramírez, J. *Angew. Chem. Int. Ed.* **2017**, *56*, 10755.

(71) Wang, Y.; Chen, Z.; Han, P.; Du, Y.; Gu, Z.; Xu, X.; Zheng, G. *ACS Catal.* **2018**, *8*, 7113.